

A Novel Asymmetric Rotor Interior Permanent Magnet Machine With Hybrid-Layer Permanent Magnets

Yang Xiao¹, Member, IEEE, Z. Q. Zhu¹, Fellow, IEEE, Geraint Wyn Jewell¹, Jintao Chen, Senior Member, IEEE, Di Wu, Member, IEEE, and Liming Gong, Senior Member, IEEE

Abstract—This article proposes a novel asymmetric interior permanent magnet (AIPM) rotor topology for torque enhancement and torque ripple reduction in IPM synchronous machines. The AIPM rotor structure is featured by a hybrid-layer permanent magnet configuration, i.e., for each pole, a part of PM configuration has one-layer while the other part has two layers. It allows the magnetic-field-shifting (MFS) effect to be utilized by reducing the current angle difference between maximum PM and reluctance torque components, thereby effectively increasing the maximum resultant torque. The proposed AIPM machine and a conventional V-shape IPM machine are designed and globally parametric optimized with the same 24-slot/4-pole stator, rotor diameter, and PM usage. The influence of key rotor geometric parameters of the AIPM machine on torque and open-circuit air-gap magnetic field characteristics are investigated. The comparison of electromagnetic performance confirms that significant torque enhancement and torque ripple reduction in the AIPM machine compared with the conventional V-shape IPM machine and reveals the MFS effect is essential for torque increase. Finally, an AIPM machine is manufactured and tested for validation.

Index Terms—Asymmetric rotor, hybrid-layer PMs, interior permanent magnet (IPM), magnetic-field-shifting (MFS), torque ripple.

I. INTRODUCTION

IN RECENT years, permanent magnet (PM) brushless synchronous machines (PMSMs) have become increasingly attractive in academia while have also been widely employed in many commercial applications [1]–[3]. In general, PMSMs can be comprehensively classified as surface-mounted and interior

Manuscript received February 22, 2021; revised June 5, 2021 and August 28, 2021; accepted September 29, 2021. Date of publication October 1, 2021; date of current version November 19, 2021. Paper 2021-EMC-0252.R2, presented at the 2020 Energy Conversion Congress and Exposition, Detroit, MI USA, Oct. 11–15, and approved for publication in the IEEE TRANSACTIONS ON INDUSTRY APPLICATIONS by the Electric Machines Committee of the IEEE Industry Applications Society. (*Corresponding author: Z. Q. Zhu.*)

Yang Xiao, Z. Q. Zhu, and Geraint Wyn Jewell are with the Department of Electronics and Electrical Engineering, The University of Sheffield, Sheffield S1 3JD, U.K. (e-mail: yxiao23@sheffield.ac.uk; z.q.zhu@sheffield.ac.uk; jewell@sheffield.ac.uk).

Jintao Chen, Di Wu, and Liming Gong are with the Midea Shanghai Motors and Drives Research Center, Shanghai 201203, China (e-mail: chenjintao@welling.com.cn; wudi9@welling.com.cn; gongliming@midea.com).

Color versions of one or more figures in this article are available at <https://doi.org/10.1109/TIA.2021.3117228>.

Digital Object Identifier 10.1109/TIA.2021.3117228

PM (IPM) machines according to the locations of PMs. Due to superior torque density, high efficiency, wide constant power speed range (CPSR), and rotor robustness [4]–[6], IPMs are preferable for variable-speed applications especially when a wide speed operation range is required, such as electric vehicles (EVs) and ships.

The enhancement of torque density and the reduction of production costs owing to expensive rare-earth PM materials are essential goals for the design of IPM machines. As the torque production in IPM machines is originated from two components: PM and reluctance torques, the increase of the reluctance torque by improving the rotor saliency can increase the resultant torque without extra PM usage, which are usually designated as PM-assisted synchronous reluctance machines (PMASRMs) in literature with multilayer rotor structures. [7] compares IPMs with single-, double-, triple-, six-, and ten-layer circular PMs. It is found that most significant increase of the maximum torque is achieved when the layer number increases from one to two. The triple-layer topology has the largest average torque but the increase in rotor saliency gradually diminishes when the number of rotor layers continues to increase. The electromagnetic performances of IPM machines with several multilayer topologies are compared in [8] and [9], including the conventional Delta-shape IPM, an improved Delta-shape IPM for Prius 2017, the double Bar-shape design used in BMW I3 and a novel three-layer IPM with mixed Delta- and U-shape structure. The comparison shows that Delta-shape IPM machine can achieve the highest average torque, while the three-layer design has lowest torque ripple and iron loss. Moreover, multilayer rotor design and cheap and sustainable ferrite PMs are employed simultaneously in IPM machines to reduce the cost while maintaining the torque density [10], [11]. Several three-layer IPM topologies using ferrite PMs are analyzed in [12] and the optimal design shows comparable average torque with a surface PM machine using rare-earth PMs. [13] proposes a novel ferrite PMASRM using the double-stator design and three-dimensional (3-D) trench air-gap to generate higher average torque than a single stator V-shape IPM using NdFeB PMs.

However, the conventional symmetrical rotor topologies in existing IPM machines result in the inherent current angle difference between maximum points of PM and reluctance torque components, which reduces utilization ratios of both torque

components at the maximum resultant torque. Therefore, a novel design concept of IPM machines has been considered by using asymmetric rotor structure to shift the maximum points of PM and reluctance torque components to be closer, which is designated as magnetic-field-shifting (MFS) effect in [14]. The principle of torque enhancement in asymmetric IPM (AIPM) machine topologies by utilizing the MFS technique is analytically analyzed in [15]. Several novel asymmetric rotor topologies employing MFS effect for torque enhancement have already been reported in literature [16]–[21]. In [16], an asymmetric IPM topology with inset PMs is proposed and the MFS effect is achieved by the shifted PM positions, which provides improvement in torque density and CPSR performance. An asymmetric topology with the hybrid rotor configuration that exhibits asymmetric inset PMs and symmetrical V-shape PMs alternatively in adjacent poles is proposed in [17] and [18]. In [19], a PM-assisted wound rotor synchronous machine is proposed that has PMs placed tangentially in the central of salient rotor poles. The novel machine shows significant increase of maximum average torque by producing higher reluctance torque and employing MFS effect. In [20] and [21], a novel V-shape IPM topology with an asymmetric flux barrier between PMs and the rotor surface in each pole has been proposed but shows negligible torque enhancement compared with the conventional V-shape design.

To utilize MFS technique for torque enhancement without extra PM usage, a novel asymmetric IPM (AIPM) rotor topology with hybrid-layer PM configuration has been proposed in [22] for IPM synchronous machines, which shows significant increase of maximum torque and reduction of torque ripple simultaneously compared with the conventional V-shape IPM machine using the same amount of the PM material. The hybrid-layer PM configuration exhibits single-layer PM in one part and double-layer PMs in the other part in each pole to utilize MFS effect. In this article, the design optimization processes of the proposed AIPM machine and a conventional V-shape IPM machine, both using the same 24-slot/4-pole stator, rotor diameter and total PM volume, have been significantly updated by considering torque ripple and mechanical stress. The investigation of effects of key geometrical parameters in the AIPM machine on torque characteristics has been extended. Compared with [22], this article has also added the comparison of inductance, cogging torque, torque ripple, demagnetization withstand capability, CPSR performance, and the analyses and comparisons of efficiency, loses and power factor between final optimal designs of AIPM and IPM machines that comprehensively reveals the merits of the proposed topology. Moreover, experimental results of the AIPM prototype are provided in this article for verification.

This article is organized as follows. Section II describes the design and optimization of the proposed AIPM machine, Fig. 1(a), and a conventional V-shape IPM machine, Fig. 1(b), with the same stator, rotor diameter and PM usage. Section III investigates the influences of basic rotor geometrical parameters of the AIPM machine on torque and open-circuit magnetic field characteristics. The electromagnetic performances of AIPM and IPM machines are compared in Section IV to confirm the

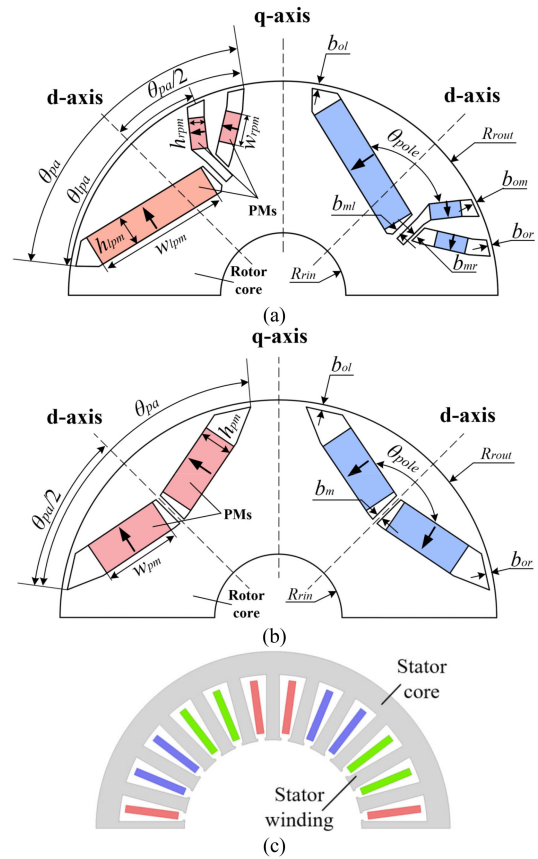


Fig. 1. Machine topologies. (a) Proposed AIPM machine using hybrid-layer PM configuration with geometrical parameters. (b) Conventional V-shape IPM machine with geometric parameters. (c) Shared 24-slot/4-pole stator design.

advantages of the proposed topology. Experimental results are reported in Section V and the conclusion is given in Section VI.

II. MACHINE TOPOLOGY AND DESIGN OPTIMIZATION

A. Proposed Machine Topology

The rotor cross sections of the proposed AIPM machine and the conventional V-shape IPM machine serving as the benchmark are shown in Fig. 1(a) and (b), respectively, while magnetization directions of PMs are denoted by arrows. The novel AIPM rotor topology is featured by the trident PM cavity and three PMs in each pole that exhibits the hybrid-layer PM configuration using PMs with different dimensions: one large-size PM and two small-size PMs. The large-size PM is buried at the single-layer part and two small-size PMs are placed separately in two holes of the double-layer part, which comprehensively forming the hybrid-layer structure to utilize MFS effect. Moreover, the same stator with three-phase single-layer 24-slot/4-pole distributed windings is shared by both machines, as illustrated in Fig. 1(c). It should be mentioned that except for the proposed topology, the proposed concept of novel AIPM topology can be extended to unequal numbers of PM layers at both sides in each pole.

The key rotor geometric parameters of the proposed AIPM and conventional IPM machines are also shown in Fig. 1(a) and (b), respectively. As shown in Fig. 1(a), the trident cavity

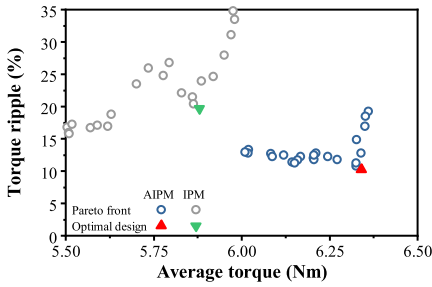


Fig. 2. Pareto fronts and optimal designs of design optimization of AIPM and IPM machines.

structure of AIPM machine in each pole has three holes for PMs, whose inner ends are located closely while outer ends are located separately and near the rotor surface. To describe the geometric positions of three outer ends and their relationships, θ_{pa} is defined to denote the reluctance pole arc between the left- and right-side holes of the trident cavity, and θ_{lpa} describes the PM pole arc between the left-side and middle holes. The widths and heights of two different types of PMs are denoted by w_{lpm} , h_{lpm} , w_{rpm} , and h_{rpm} , respectively, whereas R_{rout} and R_{rin} are the outer and inner diameters of the rotor core, respectively. For the V-shape IPM structure in Fig. 2(b), θ_{pa} is the pole arc while w_{lpm} and h_{lpm} are width and height of PMs, respectively. In Fig. 2, the position of d - and q -axis of both machines are also denoted. b_{ol} , b_{om} , b_{or} , b_{ml} , and b_{mr} are the thicknesses of iron bridges and ribs in the proposed AIPM machine while b_{ol} , b_{or} , and b_m are the iron bridge and rib thicknesses of the conventional V-shape IPM machine.

B. Design Optimization

The optimal designs of the proposed AIPM and the conventional V-shape IPM machines are obtained by global parametric optimization using genetic algorithm (GA) and 2-D time-stepping finite element (FE) analysis. The goal, constraints and conditions of the design optimization are provided as follows.

- 1) The same targets and constraints are applied for the design optimization of both machines to perform a fair comparison.
- The objective functions: Maximizing average torque using the maximum torque per ampere (MTPA) method and minimizing torque ripple, while maximizing average torque is the primary goal.
- Constraints:
 - a. Torque ripple ratio $T_{ripple} < 20\%$ at maximum average torque condition at 10 A current
 - b. Maximum irreversible demagnetization ratio $W_{de} < 5\%$ at 40 A current
 - c. Similar maximum mechanical stresses on rotor cores of AIPM and IPM machines at 6000 r/min

The torque ripple ratio and maximum irreversible demagnetization ratio are defined as follows:

$$T_{ripple} = \frac{T_{p-p}}{T_{syn}} \times 100\% \quad (1)$$

$$W_{de} = \frac{V_{irde}}{V_{mag}} \times 100\% \quad (2)$$

where T_{syn} and T_{p-p} are the average torque and the peak-to-peak torque, respectively. V_{irde} is the volume of PM regions that has smaller magnetic flux density than 0.1 T that has relatively high risk for irreversible demagnetization and V_{mag} is the total PM volume.

- 1) To ease the design optimization, some geometric restrictions are also applied for the proposed AIPM machine, as listed in the following:

$$\begin{cases} \frac{\theta_{pa}}{2} < \theta_{lpa} < \theta_{pa} \\ w_{lpm} \geq w_{rpm} \\ h_{lpm} = 2h_{rpm} \end{cases}. \quad (3)$$

- 2) Both machines use the same stator and have fixed rotor inner and outer radii, stack lamination length, and total PM volume. The same materials of core and PMs are employed for both machines. The geometric variables for optimization are dimensions of rotor cavity and PMs, Fig. 1.
- 3) For optimization of torque characteristics, the input phase current and rotor speed are fixed as 10 A(peak)/7.07 A(RMS) and 1500 r/min when current frequency is 50 Hz. For demagnetization analysis, the input phase current and rotor speed are fixed as 40 A(peak)/28.28 A(RMS) and 1500 r/min.
- 4) In the GA based optimization, 30 individuals in each population and 35 generations are applied.

The pareto fronts of both AIPM and IPM machines obtained in design optimization that satisfy the constrains of demagnetization withstand capability and mechanical strength are shown in Fig. 2. The optimal designs of both machines are selected considering both average torque and torque ripple, while maximizing average torque is the primary goal.

The final optimal designs of both AIPM and IPM machines are obtained, and some main design parameters are listed in Table I. The von-Mises stress distributions on rotor cores of both machines are compared at 6000 r/min as shown in Fig. 3. It confirms that the final optimal design of proposed AIPM machine shows similar maximum mechanical stress as that of the conventional IPM machine.

III. INFLUENCE OF KEY GEOMETRIC PARAMETERS OF PROPOSED AIPM MACHINE

In order to obtain the relationships between key rotor geometric parameters and electromagnetic performances, the influences of key geometric parameters of the proposed AIPM machine are investigated in this section based on the optimal design by employing 2-D FE analysis, with particular emphasis on torque characteristics, namely maximum average torque and torque ripple at fixed 10 A current and 1500 r/min, and open-circuit air-gap magnetic flux density distribution. Except for specifically indicated parameters, design parameters of the AIPM machine are fixed as given in Table I in the investigation of the influence of key parameters.

TABLE I
MAIN DESIGN PARAMETERS OF TOPOLOGIES

Parameters	Unit	AIPM	IPM
No. of stator slots, N_s	-		24
Pole pair number, p	-		2
Stator winding type	-	Three-phase single-layer distributed windings	
Stator outer radius	mm	50	
Axial length, L_t	mm	50	
Stator tooth width, w_s	mm	3.7	
Stator slot height, h_s	mm	18.4	
Stator slot opening, w_{so}	mm	2	
Turn number per phase, N_{ph}	-	480	
Air-gap length, δ	mm	1	
R_{rin}	mm	10	
R_{rou}	mm	24	
Total PM volume, V_{mag}	mm ³	12600	
Density of iron core	kg/m ³	7700	
Density of PMs	kg/m ³	7500	
PM material and grade	-	Nd-Fe-B, N38	
Remanence of PM at 60 °C, B_r	T	1.235	
Relative permeability of PM, μ_r	-	1.05	
Total mass of rotor core and PMs	kg	0.590	0.588
θ_{pa}	elec. degs (ED)	120	110
θ_{lpa}	ED	108	---
θ_{pole}	Mechanical degree	115	158
w_{lpm}/h_{lpm}	mm	15/3.5	--
w_{rpm}/h_{rpm}	mm	3/1.75	--
w_{pm}/h_{pm}	mm	--	8.5/3.7
b_{ol}/b_{or}	mm	0.6/0.6	0.6/0.6
b_{om}	mm	0.4	--
b_{ml}/b_{mr}	mm	0.5/0.3	--
b_m	mm	--	0.7

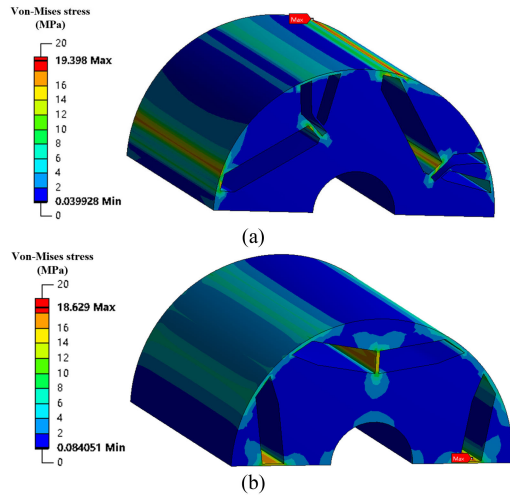


Fig. 3. Comparison of von-Mises stress distributions on rotor cores at 6000 r/min. (a) AIPM. (b) IPM.

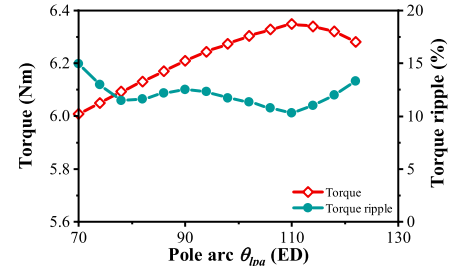


Fig. 4. Influence of pole arc θ_{lpa} on average torque and torque ripple.

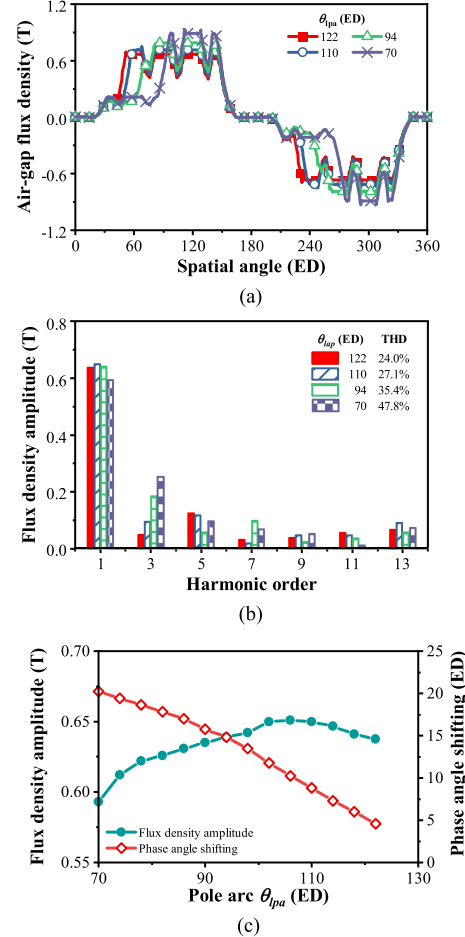


Fig. 5. Influence of pole arc θ_{lpa} on open-circuit air-gap flux density. (a) Waveforms. (b) Spectra. (c) Amplitude and phase angle shifting of fundamental flux density component.

A. PM Pole Arc θ_{lpa}

This part investigates the effects of PM pole arc θ_{lpa} on torque characteristics and open-circuit flux density when other parameters are fixed as shown in Table I. The influence of θ_{lpa} on maximum average torque and torque ripple is shown in Fig. 4. It shows that the optimal θ_{lpa} exists for maximum average torque at 110 ED. Besides, the same optimal θ_{lpa} can also achieve minimum torque ripple simultaneously.

The effect of pole arc θ_{lpa} on open-circuit air-gap flux density distributions is shown in Fig. 5. The increase of θ_{lpa} changes

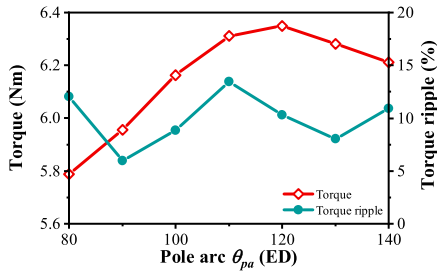


Fig. 6. Influence of pole arc θ_{pa} on average torque and torque ripple when θ_{lpa} is optimized for maximum torque in each case.

the shape of flux density distribution and eases the distortion of waveforms gradually as denoted by the total harmonic distortions (THDs). The amplitude and phase angle shifting of fundamental components of open-circuit flux-density distribution are extracted for further investigation as shown in Fig. 5(c). The phase angle shifting $\Delta\gamma$ is defined in (4) to denote the MFS effect in open-circuit flux density waveforms of AIPM machines.

$$\Delta\gamma = \gamma_{AIPM} - \gamma_{IPM} \quad (4)$$

where γ_{AIPM} and γ_{IPM} are the phase angle of fundamental components of open-circuit air-gap flux density waveforms of AIPM machine and the conventional symmetrical IPM machine, respectively.

As shown in Fig. 5(c), optimal value of θ_{lpa} exists for maximum fundamental component amplitude of flux density, and the increase of θ_{lpa} gradually reduces the phase angle shifting.

B. Reluctance Pole Arc θ_{pa}

During investigating the influence of reluctance pole arc θ_{pa} , the PM pole arc θ_{lpa} is optimized in each case for maximizing average torque at fixed 10 A, 750 r/min and MTPA, while other parameters are fixed as given in Table I. The influence of θ_{pa} on maximum average torque and torque ripple is shown in Fig. 6 when θ_{lpa} is optimized for maximum torque in each θ_{pa} case. Optimum θ_{pa} exists for maximum torque while torque ripple fluctuates with the increase of θ_{pa} . Although torque ripple at θ_{pa} for maximum torque (120 ED) is not at a high level, it can be further mitigated by selecting other θ_{pa} with the sacrifice of torque.

The effect of θ_{pa} on open-circuit air-gap flux density is shown in Fig. 7. As shown in Fig. 7(a) and (b), θ_{pa} mainly influences the pole width of flux density distribution and the increase of θ_{pa} can mitigate the distortion due to significant reduction of the third harmonic component. As to the fundamental amplitude and phase angle shifting shown in Fig. 7(c), maximum fundamental amplitude can be achieved with θ_{pa} between 90 and 120 ED, while the phase angle shifting remains similar when θ_{pa} is smaller than 100 ED but increases gradually with further increase of θ_{pa} . It is also found that the influence of θ_{pa} on open-circuit flux density, especially for the fundamental component amplitude and phase angle shifting, is relatively smaller than that of θ_{lpa} .

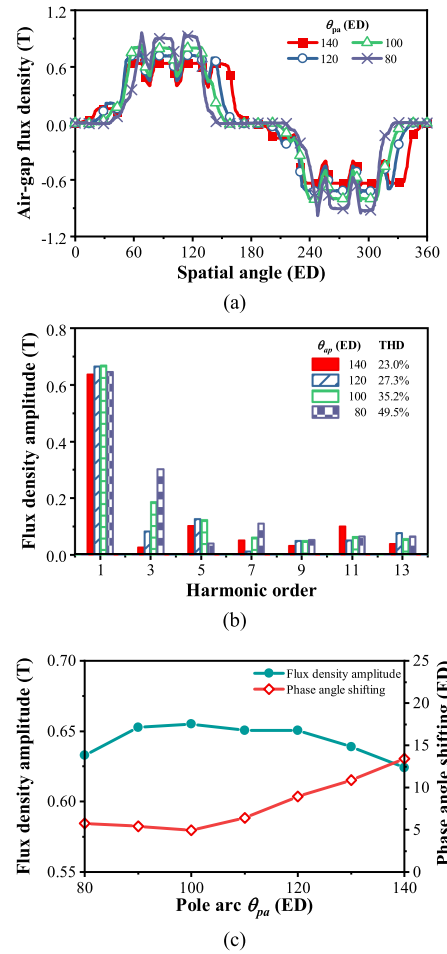


Fig. 7. Influence of pole arc θ_{pa} on open-circuit air-gap flux density when θ_{lpa} is optimized for maximum torque in each case. (a) Waveforms. (b) Spectra. (c) Amplitude and phase angle shifting of fundamental flux density component.

C. PM Width Combination

This part investigates the influence of PM width combination of PMs, namely the combination of w_{lpm} and w_{rpm} , when total PM volume and heights of PMs are fixed as given in Table I. To provide a simple description of the PM width combination, the PM width factor β_{pmw} is defined in (5), which can correspond to specific designs of PM width combination. During the investigation, both θ_{pa} and θ_{lpa} are optimized for maximizing average torque at 10 A, 750 r/min and MTPA in each case.

$$\beta_{pmw} = \frac{w_{lpm}}{w_{rpm}}. \quad (5)$$

The effects on torque characteristics and open-circuit flux density are shown in Figs. 8 and 9, respectively. Although variations of maximum average torque and torque ripple can be observed clearly with the increase of β_{pmw} and the optimum value exists, the influence of PM width combination is generally diminishing, especially on open-circuit flux density distributions due to similar spectra and THDs at different designs.

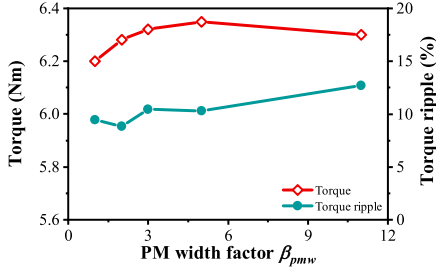
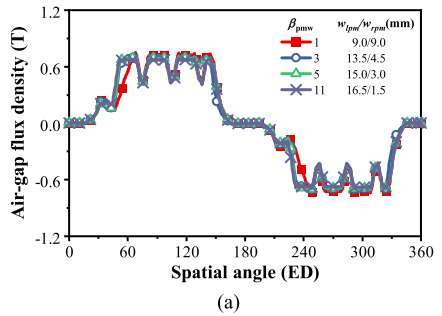
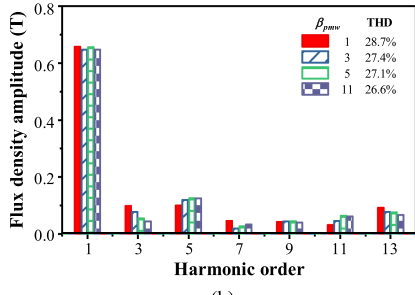


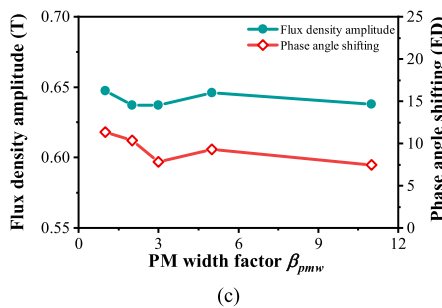
Fig. 8. Influence of PM width combination on average torque and torque ripple when θ_{pa} and θ_{lpa} are optimized for maximum torque in each case.



(a)



(b)



(c)

Fig. 9. Influence of PM width combination on open-circuit air-gap flux density when θ_{pa} and θ_{lpa} are optimized for maximum torque in each case. (a) Waveforms. (b) Spectra. (c) Amplitudes and phase angle shifting of fundamental flux density components.

IV. COMPARISON OF ELECTROMAGNETIC PERFORMANCE

This section compares the electromagnetic performances of final optimal AIPM and IPM machines obtained in Section II. B to reveal the advantages of the proposed AIPM rotor topology. The cross sections, open-circuit flux density and flux line distributions of both machines are shown in Fig. 10.

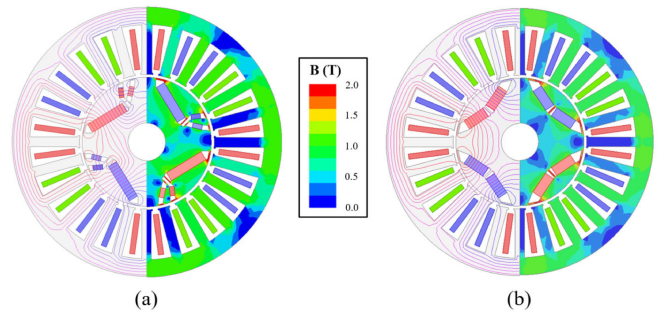
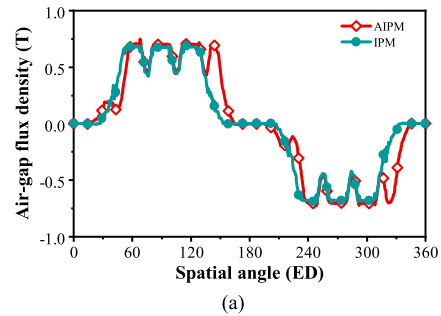
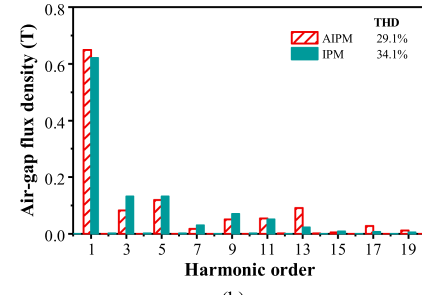


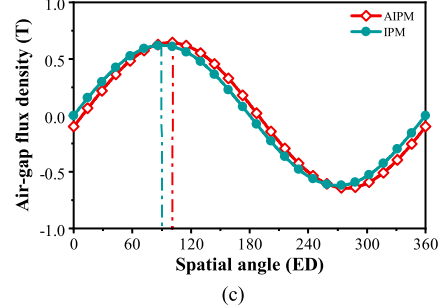
Fig. 10. Open-circuit flux density and flux line distributions of final optimal machines. (a) AIPM. (b) IPM.



(a)



(b)



(c)

Fig. 11. Comparison of open-circuit air-gap flux density. (a) Waveforms. (b) Spectra. (c) Waveforms of fundamental components.

A. Open-circuit Characteristics

The open-circuit air-gap flux density waveforms and spectra are compared in Fig. 11(a) and (b), respectively, together with waveforms of fundamental flux density component in Fig. 11(c). The axis shifting can be clearly observed in both waveforms of open-circuit air-gap flux density and its fundamental component in the AIPM machine but do not exist in the waveforms of IPM machine, which indicates MFS effect in AIPM machine. The spectra prove that the proposed AIPM machine has slightly higher amplitude of fundamental flux density component and

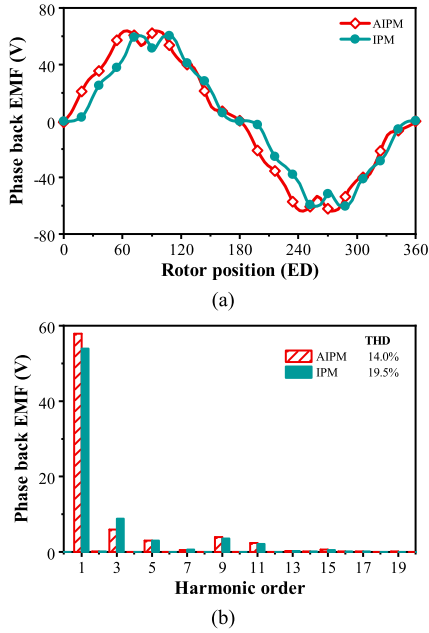


Fig. 12. Comparison of open-circuit Phase A back EMFs at 1500 r/min.
(a) Waveforms. (b) Spectra.

TABLE II
COMPARISON OF D-Q AXIS INDUCTANCES AT OPEN-CIRCUIT CONDITION

Performance	Unit	AIPM	IPM
D-axis inductance L_d	mH	21.42	18.20
Q-axis inductance L_q	mH	37.03	37.30
Cross-coupling inductance L_{dq}	mH	1.13	0.27
Saliency ratio L_q/L_d		1.73	2.05

TABLE III
COMPARISON OF KEY TORQUE PERFORMANCE

Performance	Unit	AIPM	IPM
T_{syn}^A	Nm	6.34	5.88
T_m^A	Nm	5.07	4.93
T_r^A	Nm	2.42	2.47
$\Delta\beta$	ED	48	56
TI	%	7.82	---

* T_{syn}^A , T_m^A , and T_r^A are amplitudes of average torque, PM torque, and reluctance torque, respectively; $\Delta\beta$ is the current angle difference between maximum PM and reluctance torque; TI is the torque increase ratio of AIPM machine compared with IPM benchmark; all at 1500 r/min and 10 A current amplitude.

smaller harmonic distortion due to smaller THD than IPM machine.

The waveforms and spectra of open-circuit back electromotive force (EMF) of Phase A winding are compared in Fig. 12, which also shows clear axis shifting in AIPM machine. According to the spectra, the proposed AIPM has a slightly higher amplitude of fundamental back EMF component and smaller THD of back EMF.

The inductances of both AIPM and IPM machines using d - q axis coordinates defined in Fig. 1 is compared in Table II. As can be seen, the proposed AIPM machine shows larger d -axis

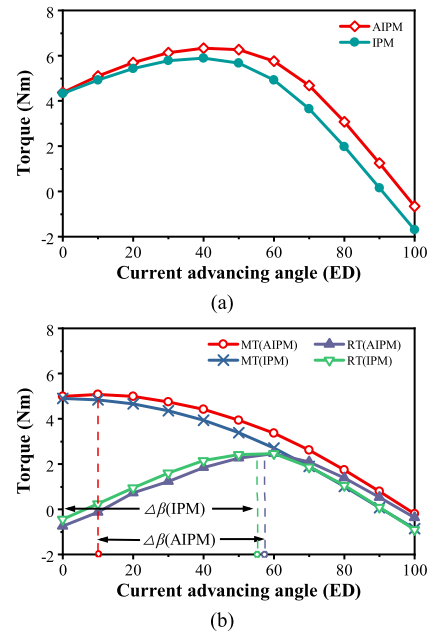


Fig. 13. Comparisons of average torque and torque components versus current advancing angle at 1500 r/min and 10 A. (a) Average torque. (b) Torque components.

inductance and smaller q -axis inductance compared with the conventional IPM machine, resulting in clearly smaller saliency ratio in AIPM machine. Besides, larger cross-coupling inductance L_{dq} is observed in AIPM machine.

B. Average torque and Torque Components

The torque performance of both machines, including average torques and torque components at 10 A current and 1500 r/min, are compared in Fig. 13 and Table III. Fig. 13(a) confirms that the proposed AIPM machine has higher maximum average torque reached at a larger current advancing angle at 10 A current compared with IPM machine. Besides, the average torque of AIPM machine reaches 0 at around 97 ED while the IPM machine reaches 0 at 90 ED, which also indicates an influence of MFS effect.

To reveal the mechanism of torque enhancement in the AIPM machine, the resultant torque is extracted into two components: PM torque and reluctance torque using frozen permeability method [23] as shown in Fig. 13(b), while torque performances are also listed in Table II. The proposed AIPM machine can achieve about 8% of torque enhancement at 10 A current compared with the optimal design of the conventional V-shape IPM machine with the same PM usage. In detail, the proposed AIPM machine can achieve slightly higher PM torque amplitude, which corresponds to the higher fundamental amplitudes of open-circuit flux density and back EMF, and slightly smaller reluctance torque amplitude, compared with the IPM machine. It should be noted that the increase of PM torque amplitude in AIPM machine is notably smaller than the increase of maximum resultant torque, although it is higher than the decrease of reluctance torque amplitude. A significant reduction of current angle difference between maximum PM and reluctance torque

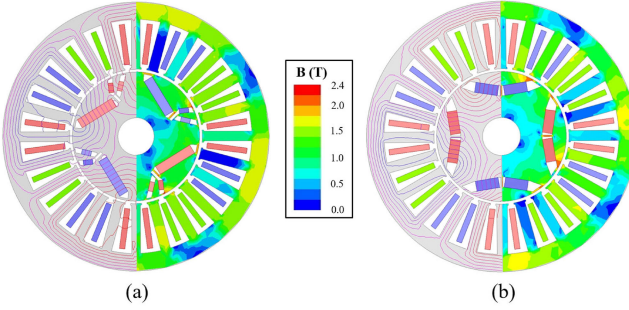


Fig. 14. Flux density and flux line distributions at 10 A, 750 r/min and MTPA. (a) AIPM. (b) IPM.

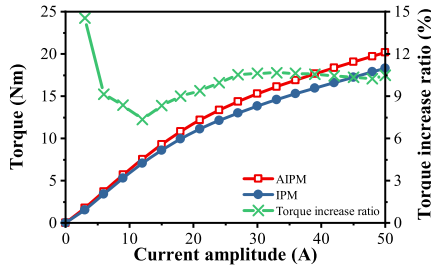


Fig. 15. Comparison of maximum average torque versus current when MTPA is applied.

components can be observed in AIPM machine compared with the IPM machine. Thus, utilizing MFS effect is essential for the torque enhancement in AIPM machine.

The flux density and flux line distributions of AIPM and IPM machines at 10 A, 750 r/min and MTPA are compared in Fig. 14. It reveals that both machines show relatively higher saturation with armature reaction compared with open-circuit conditions. The maximum average torques of both machines at 1500 r/min versus current when applying MTPA are compared in Fig. 15, which confirms the torque enhancement of the proposed AIPM machine across the wide range of current compared with the IPM machine benchmark. Approximately 10% of torque increase in average can be achieved in AIPM machine across the current range, although the torque increase ratio varies with the increase of current.

C. Torque Ripple

The waveforms of cogging torque and torque at 10 A current and 1500 r/min are compared in Fig. 16(a) and (b), respectively. Fig. 16(a) shows that AIPM machine has about 60% smaller peak-to-peak cogging torque compared with IPM machine. As confirmed in Fig. 16(b), both machines satisfy the design optimization constraints in Section II. B with torque ripple smaller than 20% at 10 A current. It is also found that significant torque ripple reduction can be achieved in AIPM machine with 10.2% torque ripple ratio, which is approximately 50% smaller than IPM machine (19.7%). Besides, torque ripple ratios at maximum average torque conditions with different current amplitudes in both machines at 1500 r/min are compared in Fig. 17, which confirms the torque ripple reduction in AIPM machine across the whole range of current compared with the IPM machine.

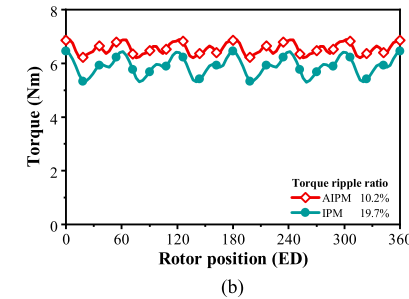
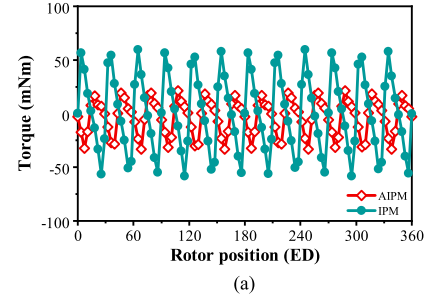


Fig. 16. Torque waveforms. (a) Cogging torque. (b) Torque waveforms at 1500 r/min, 10 A and current advancing angle for maximum torque.

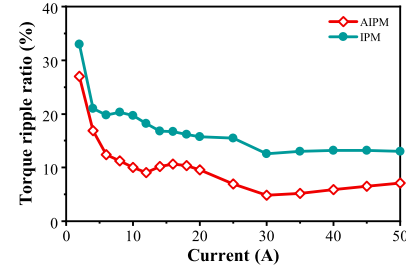


Fig. 17. Comparison of torque ripple ratios at maximum average torque conditions versus current at 1500 r/min.

D. Demagnetization Analysis

To investigate and compare the demagnetization withstand capabilities of AIPM and IPM machines, demagnetization analysis is carried out, Fig. 18(a)–(d), which investigates the PM flux density distributions with current advancing angles for maximum irreversible demagnetization in both machines at 40 A and 50 A current, respectively. The PM regions with magnetic flux density smaller than 0.1 T are considered as demagnetization area due to high irreversible demagnetization risk. As can be seen, irreversible demagnetization of PMs in both machines are negligible at 40 A but become significant at 50 A. The demagnetization ratios of both machines across the current range are compared in Fig. 18(e), which confirms that both machines satisfy the design optimization constraints in Section II. B with demagnetization ratios smaller than 5% at 40 A. It also reveals that both machines have similar demagnetization withstand capability due to similar trend of demagnetization ratio curves.

E. CPSR Performance

To compare the CPSR characteristics of two machines, the torque-speed and power-speed curves are obtained based on the method provided in [24]. The torque- and power-speed curves

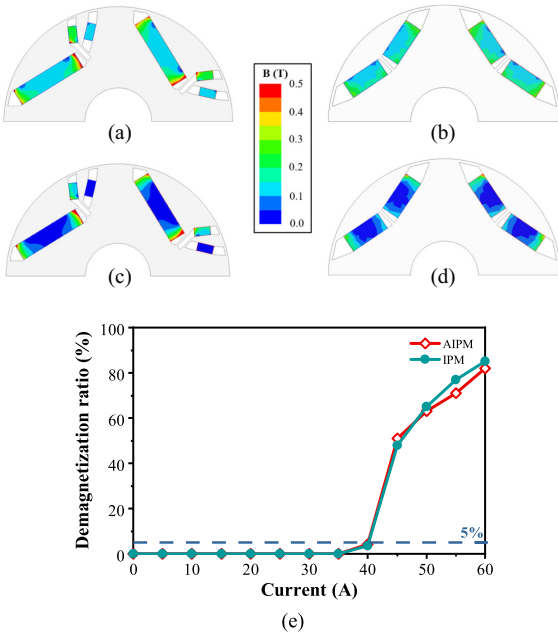


Fig. 18. Demagnetization analysis at maximum irreversible demagnetization condition at 60 °C PM temperature. (a) PM flux density distribution in AIPM at 40 A. (b) PM flux density distribution in IPM at 40 A. (c) PM flux density distribution in AIPM at 50 A. (d) PM flux density distribution in IPM at 50 A. (e) Comparison of irreversible demagnetization ratios versus current.

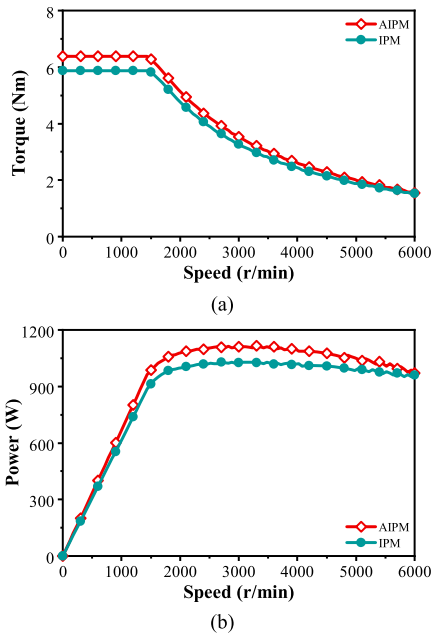


Fig. 19. Comparison of CPSR performance at maximum 10 A current, 120 V dc voltage and MTPA. (a) Torque-speed curve. (b) Power-speed curve.

at maximum current 10 A, dc bus voltage 120 V and MTPA are compared in Fig. 19. As shown in Fig. 17, the proposed AIPM machine shows significant torque and power enhancement in the constant torque region compared with the IPM machine benchmark. Although the increase of torque and power diminishes with the increase of speed, about 10% of enhancement of maximum power can be achieved by the proposed AIPM machine.

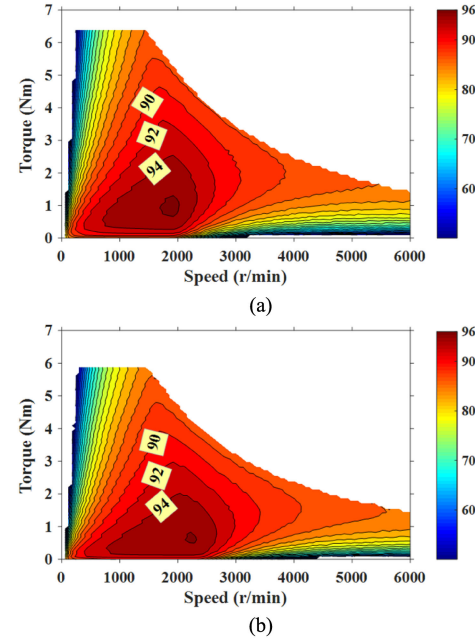


Fig. 20. Comparison of efficiency maps at maximum 10 A current, 120 V dc voltage, and MTPA. (a) AIPM. (b) IPM.

F. Efficiency, Loss, and Power Factor

The efficiency maps of both machines are also calculated considering MTPA performance based on the method in [24] as compared in Fig. 20. As can be seen, the areas of high efficiency region ($>94\%$) in both machines are generally similar. The proposed AIPM machine shows relatively higher efficiency for high torque while the conventional IPM machine has relatively higher efficiency for high speed.

The efficiency, copper and iron losses, and power factor of two machines at the same 2 Nm loading, 120 V dc voltage, 10 A maximum current and MTPA are compared in Fig. 21. Fig. 21(a) shows that the proposed AIPM machine has significantly higher efficiency at low speed, but the efficiencies of both machines at 2 Nm become similar when speed is higher than 2000 r/min and the efficiency of AIPM machine is slightly lower. It can be explained by the comparison of copper and iron losses in Fig. 21(b) and (c), respectively. As can be seen, the proposed AIPM machine shows significantly lower copper loss in the constant torque region with low speed, compared with the conventional IPM machine, but the copper losses of both machines become similar with the increase of speed in the constant power region. Besides, iron losses of both machines remain similar across the speed range at 2 Nm loading. As to power factors compared in Fig. 21(d), the proposed AIPM machine shows higher power factor at low speed while power factors of both machines are similar at high speed. Moreover, the maximum power factor of AIPM machine is higher than that of IPM machine.

V. EXPERIMENTAL VALIDATION

The final optimal design of the proposed AIPM machine has been manufactured and tested for validation with the design

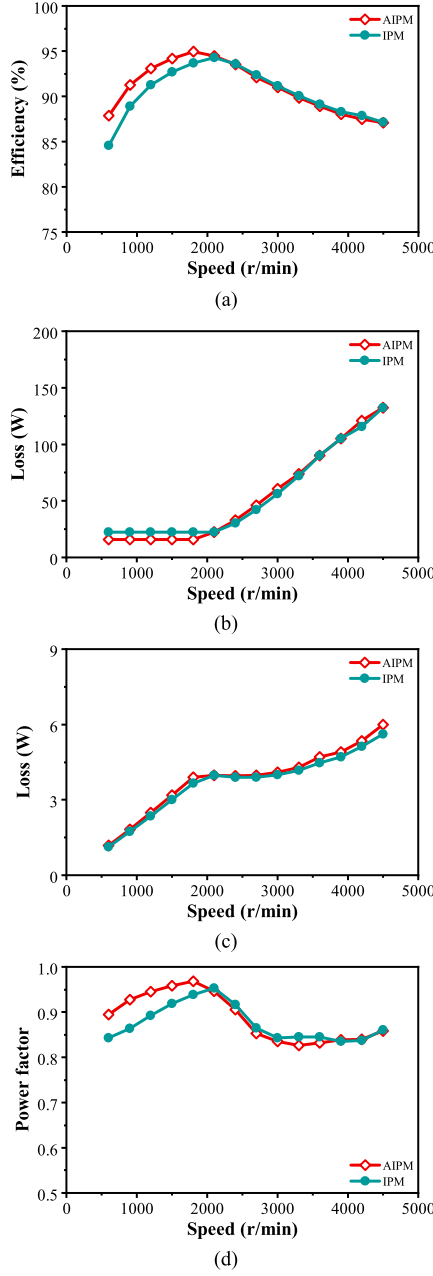


Fig. 21. Machine characteristics at 2 Nm torque loading, maximum 10 A current, 120 V dc voltage. (a) Efficiency. (b) Copper loss. (c) Iron loss. (d) Power factor.

parameters provided in Table I. Photographs of the prototype and the test platform are illustrated in Fig. 22.

The measured line back EMF waveform and spectrum at 1500 r/min are compared with the FE results in Fig. 23. It is found that the measured waveform and spectrum show good agreement with the 3-D FE-predicted results, but clear differences can be observed when comparing the measured results with the 2-D FE-predicted results because end region effects are neglected in 2-D FE analysis. Besides, the measured fundamental amplitude is about 95% and 98% of those of 2-D and 3-D FE results, respectively, while THDs of 3-D FE and measured results are similar.

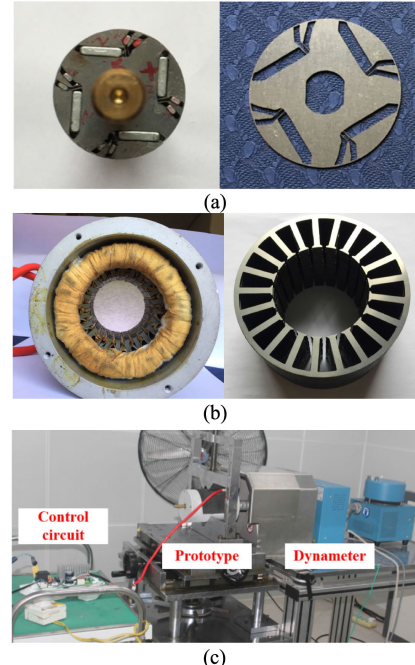


Fig. 22. Photographs of prototypes and the test platform. (a) Rotor and lamination. (b) Stator and lamination. (c) Test platform.

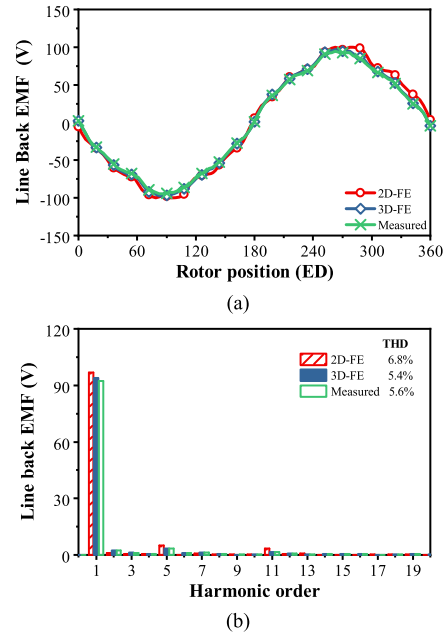


Fig. 23. Line back EMFs at 1500 r/min. (a) Waveforms. (b) Spectra.

The static torque waveforms of the prototype at different rotor position with different current are shown in Fig. 24. It is measured by maintaining the dc currents I_p in three-phase windings ($I_A = I_p$ and $I_B = I_C = -I_p/2$) while changing the relative positions between the rotor and the stator step by step. The comparison between FE and measured results also shows good match.

Fig. 25 compares the dynamic torque characteristics between 3-D FE-predicted and measured results. In Fig. 25(a), torque

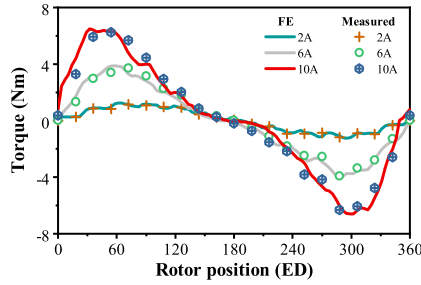


Fig. 24. Static torques versus rotor position at different currents.

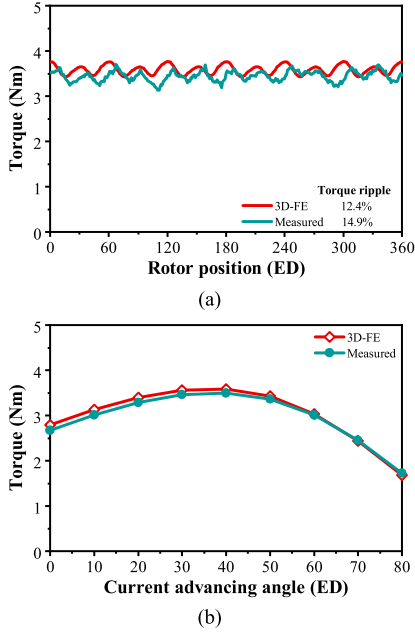


Fig. 25. Torque characteristics. (a) Dynamic torque waveforms with MTPA. (b) Average torque versus current advancing angle.

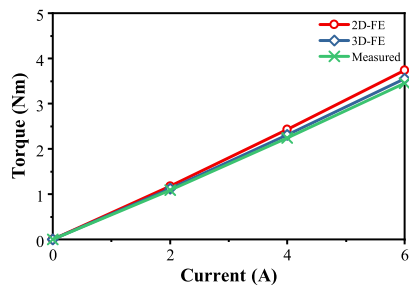


Fig. 26. Comparison of maximum torque versus current.

waveforms at 6 A and MTPA are compared, which confirms the relatively low torque ripple in the proposed AIPM machine. The comparison of torque-current advancing angle performance at 6 A is shown in Fig. 25(b).

The maximum average torque versus input current obtained by 2-D and 3-D FE simulations and dynamic torque experiments are compared in Fig. 26, while the torque values and errors at 6 A, 1500 r/min and MTPA are provided in Table IV. It also shows relatively higher error in 2-D FE analysis and good agreement between 3-D FE and measured results.

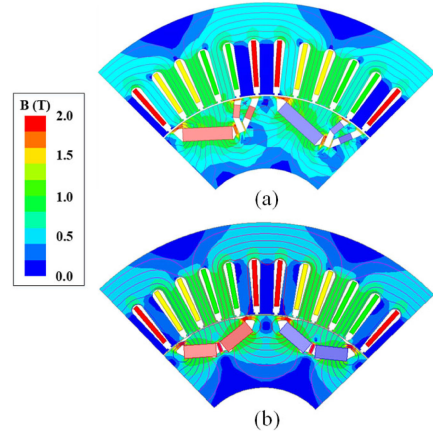


Fig. 27. Final designs and open-circuit flux density and flux line distributions of Prius 2010-scale machines. (a) AIPM. (b) IPM (Toyota Prius 2010).

TABLE V
MAIN DIMENSIONS OF TOYOTA PRIUS 2010-SCALE MACHINES

Parameters	Unit	AIPM	IPM
Number of stator slots, N_s	-	48	48
Number of turns per slot, N_c	-	11	11
Stator outer diameter, $2R_{sout}$	mm	264	264
Stator slot height, h_s	mm	31	31
Stator tooth width, w_s	mm	7.3	7.3
Winding type	-	Single-layer short-pitch winding	
Number of poles, $2p$	-	8	8
Air gap length, δ	mm	0.73	0.73
Axial length, L_t	mm	50.8	50.8
Rotor inner radius, R_{rin}	mm	45	45
Rotor outer radius, R_{rou}	mm	80.22	80.22
Total PM volume, V_{mag}	mm ³	104460	104460
Remanence of PMs, B_{res}	T	1.051	1.051
Coercivity of PMs, H_{ci}	MA/m	1.03	1.03
Width/height of large PM	mm	28.5/7.2	--
Width/height of large PM	mm	7.1/3.6	--
Width/height of PMs in IPM	mm	--	17.88/7.2
Reluctance pole arc, θ_{pa}	ED	142	128
PM pole arc, θ_{pa}	ED	111	--

TABLE IV
COMPARISON OF MAXIMUM AVERAGE TORQUE

Performance	2D FE	3D FE	Measured
Maximum torque (Nm)	3.73	3.56	3.45
Error	8.1%	3.1%	--

VI. CONCLUSION

In this article, a novel AIPM rotor topology for IPM machine featured by the trident PM cavity and hybrid-layer PMs that has one-layer PM in one part and double-layer PMs in the other part in each pole is proposed. The proposed AIPM machine can achieve significant torque enhancement and torque ripple reduction compared with the conventional V-shape IPM machine with the same stator, rotor diameter, and PM usage. The comparison by using FE analysis confirms that utilizing MFS effect has an essential role for achieving the increase of torque

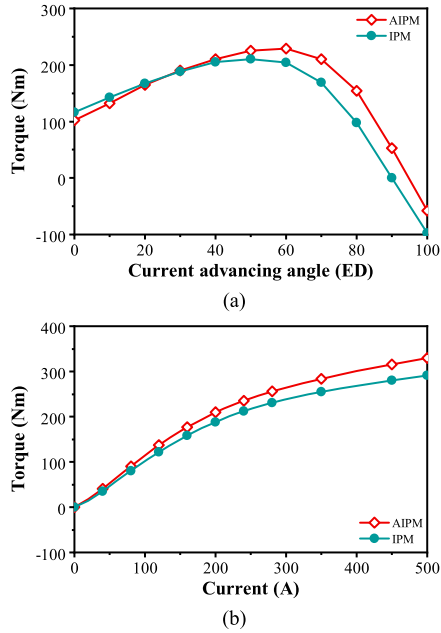


Fig. 28. Comparison of torque characteristics. (a) Torque-current angle characteristics at 236 A current and 750 r/min. (b) Maximum torque versus current with MTPA at 750 r/min.

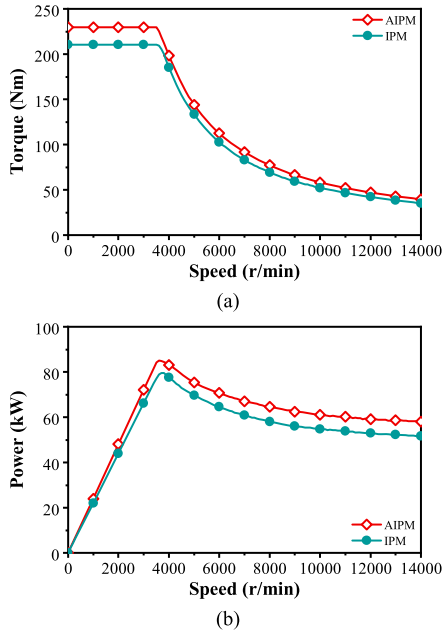


Fig. 29. CPSR performance. (a) Torque-speed curves. (b) Power-speed curves.

density. Finally, experimental results of the AIPM prototype are provided for verification.

Due to the advantages of the proposed AIPM machine compared with the V-shape IPM machine, including significant torque/power enhancement across the wide speed range, reduction of torque ripple and cogging torque, similar mechanical strength, efficiency and loss performance, the proposed AIPM machine topology shows potential for EV and hybrid EV (HEV) applications, considering the relatively simple structure using

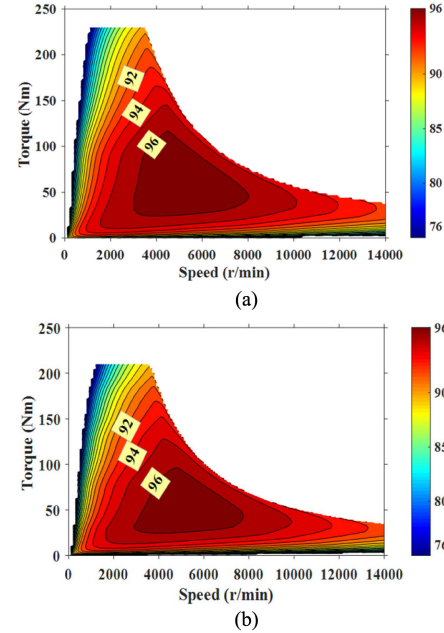


Fig. 30. Comparison of efficiency maps. (a) AIPM. (b) IPM.

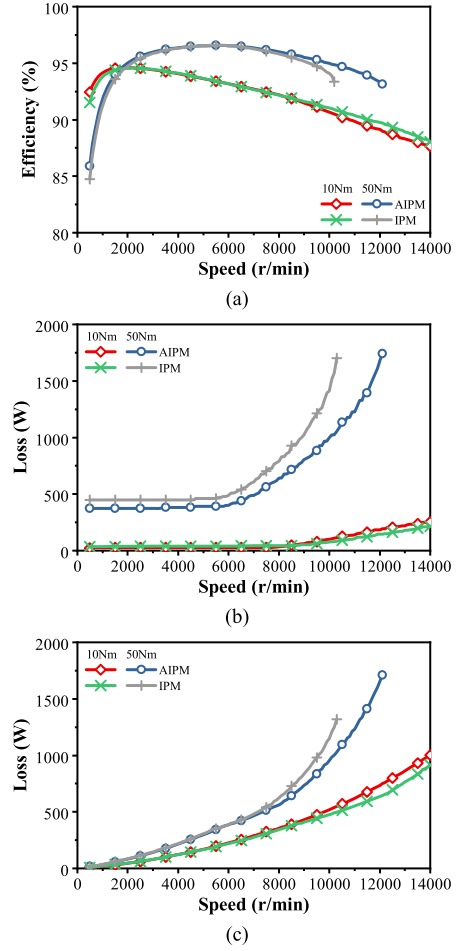


Fig. 31. Comparison of efficiency and losses at light loads. (a) Efficiency. (b) Copper loss. (c) Iron loss.

only three pieces of PMs per pole that will not causing issues for manufacturability.

Although the investigated machines in this article only have 4 poles, the proposed rotor topology remains the torque enhancement for machines with higher number of poles that is usually employed in commercial EV machines, e.g., $2p$ is 6, 8, 10, and 12. It is confirmed by the comparison of EV-scale cases using 8 pole numbers in the Appendix.

The proposed hybrid-layer structure can also be employed to develop novel multilayer AIPM topologies by mixing with other structures, e.g., mixed hybrid-layer and V-shape topology and mixed hybrid-layer and double-V shape topology. However, these multilayer AIPM topologies may be more complicated mechanically.

APPENDIX

To investigate the benefits and limitations of the proposed AIPM machine topology for EV/HEV applications, an AIPM machine employing the proposed topology is designed using the same 48-slot/8-pole stator, airgap, rotor diameter, and total PM amount to the IPM machine for Toyota Prius 2010 [25]. The final designs of both AIPM and IPM machines and their open-circuit flux density and flux line distributions are shown in Fig. 27. The main dimensions of both Prius-scale machines are provided in Table V.

Fig. 28 compares the torque characteristics of both machines. As can be seen, the proposed AIPM machine has significant torque enhancement across the investigated current range. The CPSR performances of AIPM and IPM machines with 650 V dc voltage and 236 A maximum current amplitude are shown in Fig. 29. It confirms the increase of torque and power with the same PM usage in the proposed AIPM machine across the wide speed range compared with the Toyota Prius 2010 machine.

The efficiency maps along the torque-speed curves of AIPM and IPM machines are compared in Fig. 30. The AIPM machine shows clearly larger high efficiency regions ($> = 96\%$) than the IPM machine benchmark, particularly in the regions with relatively high torque due to the torque enhancement.

To compare the efficiency and losses of AIPM and IPM machines especially at light loads, the efficiency, copper loss, and iron loss of both machines at 10 and 50 Nm output torques with the same constraints for CPSR performance calculation are shown in Fig. 31. At 50 Nm load, the efficiency of AIPM machine across the speed range remains relatively higher than that of the IPM machine. Moreover, AIPM machine has clearly lower copper loss than IPM machine across the speed range while also shows lower iron loss especially at high speed. At light 10 Nm load, the AIPM machine has slightly higher efficiency, slightly smaller copper loss, and similar iron loss than the IPM machine benchmark at low and medium speed (< 8000 r/min). However, at high speed of 10 Nm load, AIPM machine shows smaller efficiency due to higher copper loss and iron loss, in particular the iron loss, than the IPM machine benchmark.

REFERENCES

- [1] Z. Zhu and D. Howe, "Electrical machines and drives for electric, hybrid, and fuel cell vehicles," *Proc. IEEE*, vol. 95, no. 4, pp. 746–765, Apr. 2007.
- [2] K. Chau, C. C. Chan, and C. Liu, "Overview of permanent-magnet brushless drives for electric and hybrid electric vehicles," *IEEE Trans. Ind. Electron.*, vol. 55, no. 6, pp. 2246–2257, May 2008.
- [3] H. Zhang, W. Hua, Z. Wu, and X. Zhu, "Design considerations of novel modular-spoke-type permanent magnet machines," *IEEE Trans. Ind. Appl.*, vol. 54, no. 5, pp. 4236–4245, May 2018.
- [4] I. Boldea, L. N. Tutelea, L. Parsa, and D. Dorrell, "Automotive electric propulsion systems with reduced or no permanent magnets: An overview," *IEEE Trans. Ind. Electron.*, vol. 61, no. 10, pp. 5696–5711, Jan. 2014.
- [5] Z. Q. Zhu, W. Q. Chu, and Y. Guan, "Quantitative comparison of electromagnetic performance of electrical machines for HEVs/EVs," *CES Trans. Electr. Mach. Syst.*, vol. 1, no. 1, pp. 37–47, Jul. 2017.
- [6] Z. S. Du and T. A. Lipo, "Efficient utilization of rare earth permanent-magnet materials and torque ripple reduction in interior permanent-magnet machines," *IEEE Trans. Ind. Appl.*, vol. 53, no. 4, pp. 3485–3495, Jul./Aug. 2017.
- [7] Y. Honda, T. Higaki, S. Morimoto, and Y. Takeda, "Rotor design optimisation of a multi-layer interior permanent-magnet synchronous motor," *IEEE Proc. Electr. Power Appl.*, vol. 145, no. 2, pp. 119–124, Mar. 1998.
- [8] Y. Hu, S. Zhu, C. Liu, and K. Wang, "Electromagnetic performance analysis of interior PM machines for electric vehicle applications," *IEEE Trans. Energy Convers.*, vol. 33, no. 1, pp. 199–208, Mar. 2018.
- [9] S. Zhu, W. Chen, M. Xie, C. Liu, and K. Wang, "Electromagnetic performance comparison of multi-layered interior permanent magnet machines for EV traction applications," *IEEE Trans. Magn.*, vol. 54, no. 11, pp. 1–5, Nov. 2018.
- [10] S. S. Maroufian and P. Pillay, "Design and analysis of a novel PM-assisted synchronous reluctance machine topology with Alnico magnets," *IEEE Trans. Ind. Appl.*, vol. 55, no. 5, pp. 4733–4742, Sep./Oct. 2019.
- [11] H. Cai, B. Guan, and L. Xu, "Low-cost ferrite PM-assisted synchronous reluctance machine for electric vehicles," *IEEE Trans. Ind. Electron.*, vol. 61, no. 10, pp. 5741–5748, Oct. 2014.
- [12] M. Barcaro and N. Bianchi, "Interior PM machines using ferrite to replace rare-earth surface PM machines," *IEEE Trans. Ind. Appl.*, vol. 50, no. 2, pp. 979–985, Mar./Apr. 2014.
- [13] K. Kondo, S. Kusase, T. Maekawa, and K. Hanada, "A new PM-assisted synchronous reluctance motor with three-dimensional trench air gap," *IEEE Trans. Ind. Appl.*, vol. 50, no. 4, pp. 2485–2492, Jul./Aug. 2014.
- [14] Y. Xiao, Z. Q. Zhu, J. T. Chen, D. Wu, and L. M. Gong, "A novel interior permanent magnet synchronous machine," in *Proc. Int. Conf. Electr. Mach.*, Gothenburg, Sweden, 2020, pp. 26–32.
- [15] Z. Q. Zhu and Y. Xiao, "Novel magnetic-field-shifting techniques in asymmetric rotor pole interior PM machines with enhanced torque density," *IEEE Trans. Magn.*, early access, doi: [10.1109/TMAG.2021.3076418](https://doi.org/10.1109/TMAG.2021.3076418).
- [16] J. Y. Alsawalhi and S. D. Sudhoff, "Design optimization of asymmetric salient permanent magnet synchronous machines," *IEEE Trans. Energy Convers.*, vol. 31, no. 4, pp. 1315–1324, Dec. 2016.
- [17] G. Liu, G. Xu, W. Zhao, X. Du, and Q. Chen, "Improvement of torque capability of permanent-magnet motor by using hybrid rotor configuration," *IEEE Trans. Energy Convers.*, vol. 32, no. 3, pp. 953–962, Feb. 2017.
- [18] G. Xu, G. Liu, W. Zhao, Q. Chen, and X. Du, "Principle of torque-angle approaching in a hybrid rotor permanent-magnet motor," *IEEE Trans. Ind. Electron.*, vol. 66, no. 4, pp. 2580–2591, Jun. 2018.
- [19] W. Chai, H. Yang, F. Xing, and B. Kwon, "Analysis and design of a PM-assisted wound rotor synchronous machine with reluctance torque enhancement," *IEEE Trans. Ind. Electron.*, vol. 68, no. 4, pp. 2887–2897, Apr. 2021.
- [20] T. Takahashi, Y. Miyama, M. Nakano, and K. Yamane, "Permanent magnet rotating electric machine," Japan and PCT Patent Appl. WO 2019/064801 A1, Apr. 2019.
- [21] K. Yamazaki and R. Kondo, "Reduction of cross magnetization in interior permanent magnet synchronous motors with V-shape magnet configurations by optimizing rotor slits," in *Proc. IEEE Energy Convers. Congr. Expo.*, Baltimore, MD, USA, 2019, pp. 4873–4879.
- [22] Y. Xiao, Z. Q. Zhu, J. T. Chen, D. Wu, and L. M. Gong, "A novel asymmetric rotor interior PM machine with hybrid-layer PMs," in *Proc. IEEE Energy Convers. Congr. Expo.*, Detroit, MI, USA, 2020, pp. 2286–2291.
- [23] Z. Q. Zhu and W. Q. Chu, "Advanced frozen permeability technique and applications in developing high performance electrical machines," *Trans. China Electrotech. Soc.*, vol. 31, no. 20, pp. 13–29, Oct. 2016.

- [24] W. Q. Chu, Z. Q. Zhu, J. Zhang, X. Liu, D. A. Stone, and M. P. Foster, "Investigation on operational envelopes and efficiency maps of electrically excited machines for electrical vehicle applications," *IEEE Trans. Magn.*, vol. 51, no. 4, pp. 1–10, Apr. 2015.
- [25] T. A. Burress *et al.*, "Evaluation of the 2010 Toyota Prius hybrid synergy drive system," Tech. Rep. ORNL/TM2010/253, Oak Ridge Nat. Lab., Oak Ridge, TN, USA, 2010.



Yang Xiao (Member, IEEE) received the B.Eng. and Ph.D. degrees in electrical engineering from the Huazhong University of Science and Technology, Wuhan, China, in 2013 and 2018, respectively. Since 2018, he has been working toward the second Ph.D. degree in electronic and electrical engineering with The University of Sheffield, Sheffield, U.K.

His current research interests include the design of permanent magnet machines.



Z. Q. Zhu (Fellow, IEEE) received the B.Eng. and M.Sc. degrees from Zhejiang University, Hangzhou, China, in 1982 and 1984, respectively, and the Ph.D. degree from The University of Sheffield, Sheffield, U.K., in 1991, all in electrical and electronic engineering.

Since 1988, he has been with The University of Sheffield, where he is currently a Professor with the Department of Electronic and Electrical Engineering, the Head of the Electrical Machines and Drives Research Group, the Royal Academy of Engineering/Siemens Research Chair, the Academic Director of Sheffield Siemens Gamesa Renewable Energy Research Centre, the Director of Midea Electrical Machines and Control Systems Research Centres, and the Director of Sheffield CRRC Electric Drives Technology Research Centre. His current major research interests include the design and control of permanent-magnet brushless machines and drives for applications ranging from electrified transportation through domestic appliance to renewable energy.

Dr. Zhu was the recipient of 2019 IEEE Industry Applications Society Outstanding Achievement Award and the 2021 IEEE Nikola Tesla Award. He is a Fellow of the Royal Academy of Engineering and the IET, U.K.



Geraint Wyn Jewell received the B.Eng. and Ph.D. degrees in electrical engineering from The University of Sheffield, Sheffield, U.K., in 1988 and 1992, respectively.

Since 1994, he has been a Member of Academic Staff with the Department of Electronic and Electrical Engineering, The University of Sheffield, where he is currently a Professor of Electrical Engineering, the Head of the Department, and the Director of the Rolls-Royce University Technology Centre in Advanced Electrical Machines. He held an Engineering and Physical Sciences Research Council Advanced Research Fellowship from 2000 to 2005 and a Royal Society Industry Fellowship with Rolls-Royce from 2006 to 2008. His research interests include the modeling and design of a wide variety of electromagnetic devices, notably electrical machines for aerospace and high-temperature applications.



Jintao Chen (Senior Member, IEEE) received the B.Eng. and M.Sc. degrees from the Huazhong University of Science and Technology, Wuhan, China, in 2001 and 2004, respectively, and the Ph.D. degree from The University of Sheffield, Sheffield, U.K., in 2009, all in electrical engineering.

From 2004 to 2006, he was an Engineer with Delta Electronics (Shanghai) Company, Ltd., Shanghai, China. He is currently a General Manager of Midea Automotive Components, Ltd., and also with the Midea Shanghai Motors and Drives Research Center, Shanghai, China. His major research interests include the design of permanent magnet machines.



Di Wu (Member, IEEE) received the M.Sc. degree in electrical engineering from the Huazhong University of Science and Technology, Wuhan, China, in 2011, and the Ph.D. degree in electronic and electrical engineering from The University of Sheffield, Sheffield, U.K., in 2015.

Since 2011, he has been working with the Midea Welling Motor Technology (Shanghai) Co., Ltd., Shanghai, China, and is currently the Head of Motor Development Department, Welling, Midea Group. His major research interests include the design and analysis of permanent-magnet brushless machines.



Liming Gong (Senior Member, IEEE) received the B.Eng. and M.Sc. degrees in electrical engineering from the Huazhong University of Science and Technology, Wuhan, China, in 2001 and 2004, respectively, and the Ph.D. degree in electrical and electronic engineering from The University of Sheffield, Sheffield, U.K., in 2012.

Since 2012, he has been with the Midea Welling Motor Technology (Shanghai) Co., Ltd., Shanghai, China. He is currently a General Manager of Servotronics Motion Control Company, Midea Group. His research interests include control of permanent-magnet brushless machines and power electronics.